Synthesis of prussian blue analog (Co/TCNi/HCCr) nanoparticles using a facile co-precipitation approach and evaluation of their dielectric characteristics for electronic applications

S. Mosaad[1],* , Ahmed H. Ibrahim[1], E. Elesh[2], D. G. El-Damhogi[3], and Elsayed Elgazzar[1]

[1] Department of Physics, Materials Science Laboratory, Faculty of Science, Suez Canal University, Ismailia 41511, Egypt

[2] Department of Physics, Faculty of Science, Port Said University, Port Said 41522, Egypt

[3] Department of Physics and Mathematical Engineering, Faculty of Engineering, Port Said University, Port Fouad 42526, Egypt

ABSTRACT

The Prussian blue analog $Co_{0.4}/(TCNi)_{0.2}/(HCCr)_{0.6}$ (PBA) nanoparticles were synthesized via a chemical co-precipitation approach. The structural characteristics of the nanocomposite (NCp) were investigated using the XRD technique, which revealed that the synthetic PBA has a tiny crystallite size and poor crystallinity. The XRD analysis suggests that the fabricated NCp has a face-centered cubic structure with space group Fm-3 m. For deep microstructure analysis, SEM, EDX, and AFM were employed to describe the topological nature and surface architecture. It is observed that the PBA nanocomposite has a small crystallite size of ~13.66 ± 0.32 nm. The particles' surface displays a high degree of homogeneity, while the grain boundaries are clearly discernible, presenting a spherical morphology with an average diameter of 22 ± 2.1 nm. The porosity was ascertained from an AFM image of approximately 140. Furthermore, the value of the average roughness (R_s) is 6.86 nm. The AC conductivity of PBA in disc form was calculated at various temperatures and frequencies. The results indicate that the dielectric constant (ε') of PBA nanoparticles exhibits a rise from 163 to 3464 throughout the frequency range of 10–100 kHz at ambient temperature and from 27 to 6000 at 293 K. This finding provides confirmation that the dielectric characteristics of PBA nanoparticles are enhanced during the process of annealing. The values of the exponent factor (s) range from 0 to 1; this behavior is connected to the correlated barrier hopping model (CBHM) for AC conductivity. The value of W_M was ascertained to be 1.69 eV. Furthermore, the values of activation energy were calculated, and these values decreased from 0.20 to 0.17 eV with annealing. The change in loss tangent (tanδ) as a function of angular frequency at various temperatures is

Address correspondence to E-mail: sara_mosaad@science.suez.edu.eg

E-mail Addresses: ahmed_abdel-hamid@science.suez.edu.eg; eman_phs@yahoo.com; Dinagalal42@yahoo.com; elsayed.elgazzar@yahoo.com

Ⓐ Springer

also shown. The investigation of the dielectric characteristics was measured over a wide range of frequencies and temperatures to get valuable data about the dissipation properties of the prospective electronic applications.

1 Introduction

Nanotechnology is the use of nanoscale items in several disciplines of science and engineering. The highly specialized and carefully regulated physical and chemical properties of ceramics, especially iron-based nanoparticles (NPs), have been developed [1]. An impressive amount of interest has grown in the production and application of nanoscale iron oxide-based materials during the past few years in the field of electronics [1, 2]. However, high active losses caused by eddy currents are a severe disadvantage of most metals and alloys in electronic applications. Some classes of metal oxides, such as Hexaferrites and spinel ferrites, have excellent microwave characteristics, are robust in tough conditions, and do not have such an issue [3, 4]. Prussian blue (PB) got its name in the 18th century when this composition was employed to color the Prussian army's uniforms. During that time, the dark blue pigment was given various names, including Berlin, Parisian, and Turnbull's blue [5]. It was utilized in numerous creative processes, including painting, printing, and dyeing, as a color pigment. Prussian blue Analogs (PBAs), commonly known as hexacyanometallates (HCM), are compositions based on iron ions (Fe^{2+} or Fe^{3+}) with the empirical formula $A_x M_y[B(CN)_6] \cdot n H_2O$, where M and B are transition metals, which consist of blinking $B^{III}N_6$ and $B^{II}C_6$ octahedra, A is the alkaline ion, x and y are a stoichiometric factors, and n is the number of water molecules [6]. Cyanoferrates usually show a crystalline structure of cubic symmetry with space group Pm-3 m. In this structure, Fe^{3+} is coordinated by six N atoms in an octahedral arrangement, while Fe^{2+} is coordinated by six C atoms in an octahedral arrangement. The octahedral occupancies of $[B^{III}N_6]$ and $[B^{II}C_6]$ exhibit imperfections due to the possibility of vacancies, and the charges are altered by oxygen atoms originating from host H_2O molecules present in the lattice framework or interstitial sites situated among the octahedra of the unit cell itself. Several PBAs might even show distinct colors, but they could no longer be blue. Many PBAs can have solvent residuals partially filling one of the two locations. Furthermore, it is common for these PBA materials to possess a substantial quantity of water molecules, with a significant portion occupying interstitial positions between the octahedral units. However, some oxygen atoms from the water molecules may also be located at conventional sublattices to maintain the charge neutrality of the constituent ions. Due to their distinctive qualities, Prussian blue analogs (PBAs) are a class of materials that have recently attracted a lot of interest [7]. Several of these traits make PBAs particularly suitable for energy storage. Since the 18th century, Prussian blue and its counterparts, known as Prussian blue analogs (PBAs), have been used for biosensors [8], saltwater desalination [9], and hydrogen storage [10]. Due to their distinctive qualities, such as their high theoretical specific capacity, usage of synthesis, and low cost, PBAs are becoming increasingly attractive in the field of energy storage [9]. PBAs were also utilized in secondary batteries that transmitted charge using cations other than sodium. PBAs have a promising future in lithium-ion batteries (LIBs), multivalence ion batteries, and potassium ion batteries (KIBs) because of their abundant interstitial sites, which can store almost all alkali metals, including multivalence metals like Mg, Ca, Zn, and Al [10]. PBA composites exhibit superb optical [11, 12], opto-magnetic [13], catalytic [14], and electric [15, 16] characteristics, and they have recently fascinated the interest of many researchers for their dielectric properties as well. The investigation of the real part of permittivity assists with comprehending the mechanisms of metal-to-metal charge transport in PBAs [17]. Furthermore, distinctions in the real part of permittivity are useful for storage devices' potential applications [9]. D.H.M. Buchold et al. [18] and Ohkoshi et al. [19] performed investigations on the dielectric characteristics of Fe–Mn PBA materials, considering the aforementioned factors. They demonstrated that the Mn^{2+}–NC–Fe^{3+} octahedral unit in Fe–Mn PBAs behaves differently than that of the Mn^{3+}–NC–Fe^{2+} unit. Simultaneously, PBAs-based Fe–Co is being developed as a photo-induced magnetic material in PBAs, bringing PBAs to a recent research peak. It is well known that novel composite materials, which have recently attracted significant technical attention, are produced by combining several compounds with exceptional electrical characteristics. The inclusion of

a second phase can greatly improve the electric and dielectric characteristics of the composite material, as has been reported in many works [20, 21]. It is also possible to fabricate novel hybrid composites with improved and appealing electric properties by mixing various types of polymers with oxides and carbon-based compositions [22, 23]. Tuning the shapes and sizes of nanoparticles, on the other hand, is a key goal in today's modern chemical synthesis and material science [24–26]. Several researchers are striving hard to control the growth of PBAs. Various chemical approaches were used to synthesize these types of NCPs, including solution growth [18], microemulsion [27], co-precipitation route [28, 29], film deposition [30], hydrothermal synthesis [31], and sonochemical synthesis [32]. PBAs were also developed in an array of shapes, including nanosphere, film, nanowire, nanotube, nanocube, and hollow nanotube [32].

The current study presented the synthesis of a novel PBA [CoTCNi/HCCr] via direct chemical reaction without requiring a base like NaOH or NH₄OH. So, the synthesis of PBA with high porosity, huge surface area, and tiny particle size is the first goal of the study. PBA [CoTCNi/HCCr] generally has outstanding structural–morphological properties that make it suitable for use in a variety of electrical applications and energy storage. Due to a lack of research on PBA in the electrical field, it is crucial to investigate this material at the specified frequencies and temperatures. The primary aim of this report is to identify its structural characteristics and then estimate its AC electrical parameters. In addition, this article focused on studying AC electrical conductivity, the electron transfer processes in the system under consideration, and how to compute the system's parameters depending on each process. Alternating current is utilized because it makes it possible to assess a material's conductivity with greater accuracy. Additionally, the use of AC makes it possible to test a material's conductivity over a broad frequency range and identify the charge transport mechanism, both of which can yield more precise details about a material's characteristics.

2 Experimental details

2.1 Materials and chemicals

PBA [$Co_{0.4}$/$(TCNi)_{0.2}$/$(HCCr)_{0.6}$] was prepared using Potassium hexacyanochromate (III) [$K_3Cr (CN)_6$, min

98], Potassium tetracyanonickelate (II) [$KNi(CN)_4$, min 96], Cobalt chloride dihydrate [$CoCl_2.2H_2O \geq 097.0\%$] (Alfa easer, Germany), and Ethanol, Acetone (Fisher Scientific, England).

2.2 Synthesis of the prussian blue analog (PBA) by co-precipitation technique

Various chemical and electrochemical techniques were used to obtain fine NPs, especially PBA, including solution growth [18], microemulsion [27], co-precipitation pathway [24, 25, 28, 29], film deposition [30], hydrothermal synthesis [31], and sonochemical synthesis [32]. For PBA [$Co_{0.4}$/$(TCNi)_{0.2}$/$(HCCr)_{0.6}$] fabrication, firstly, 3.560 g [$K_3Cr(CN)_6$] was dissolved in 40 ml deionized water, and 2.165 g [$KNi(CN)_4$] was dissolved separately in 30 ml deionized water for 2 h at room temperature with the magnetic stirrer. Second, the aqueous solutions were mixed with continuous stirring for 3 h at a steady pace. 1.150 g $CoCl_2.2H_2O$ was dissolved in deionized water and then added dropwise to cyanide salt solution with continuous stirring for 5 h at room temperature. A homogenous precipitate powder was produced at pH ~ 9. Following that, the precipitate was separated using filter paper and washed several times with double distilled water to remove the unreacted ion salts. After that, it dried in an oven at 80 °C for 12 h and finally annealed in a muffle furnace at 180 °C for 5 h. The synthesized PBA powder was pressed into a disc shape with a radius of 0.74 cm and a thickness of 1.95 mm to be utilized without any further purification or processing for AC measurements.

2.3 Experimental techniques

The phase and crystallographic parameters of the prepared PBA were investigated using a conventional X-ray diffraction (XRD; Rigaku Smart Lab.) of CuKα radiation (λ = 1.54056 Å) at 2θ angle varied from 5°–70°, at a counting rate of 2° (2θ)/min per step. Energy-dispersive X-ray analysis (EDX) was utilized to record the elemental and purity of the composition. For further microstructure analysis, scanning electron microscopy (SEM; Helios Nanolab. 400) and atomic force microscopy (AFM Park System, 212) were performed to investigate the surface morphology and topological nature. The dielectric properties of the PBA pressed disc were evaluated using BDS-40 wide-band dielectric spectroscopy throughout a temperature

Fig. 1 a The XRD pattern of the Prussian blue analog CoTCNi/HCCr, **b** EDX spectrum of the Prussian blue analog CoTCNi/HCCr
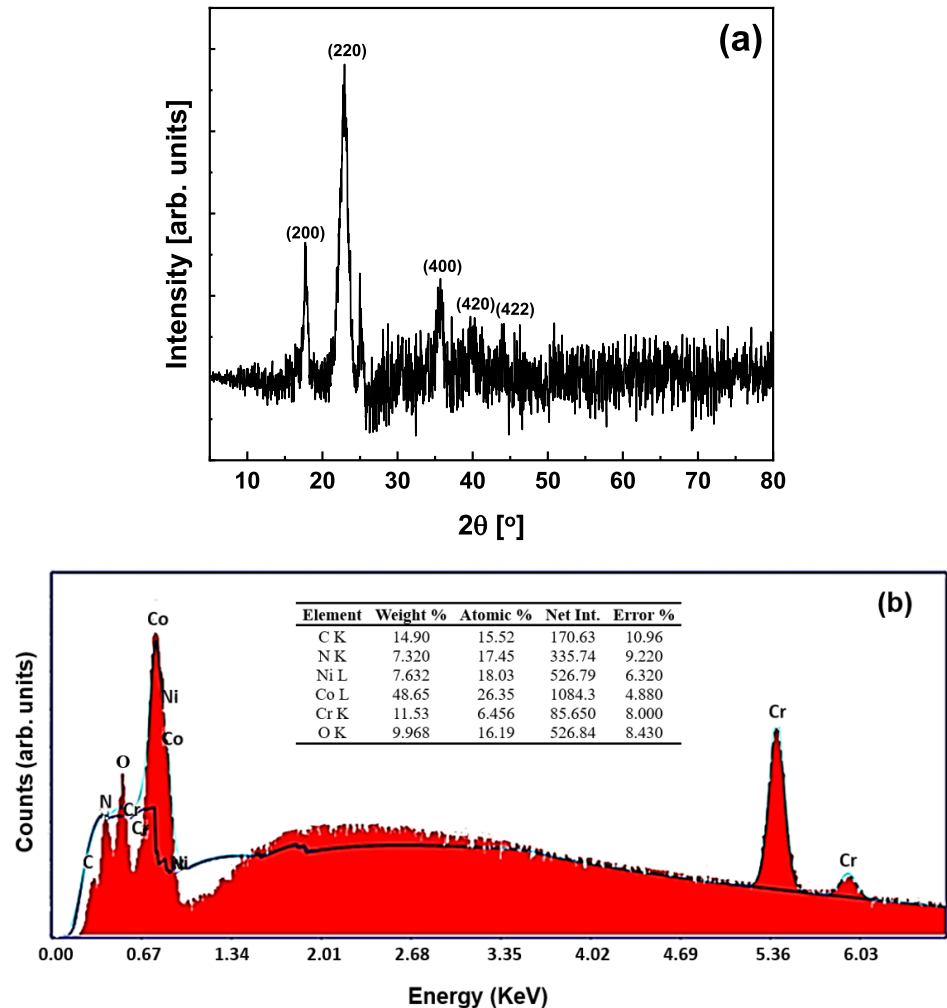
range of 293–373 K. In this approach, a high-resolution Alpha analyzer with a specimen head (Novocontrol Technologies GmbH) was used. The experiment was performed with a 20 K step and a frequency range of 10 Hz–100 kHz.

3 Results and discussion

3.1 Microstructure and topological analysis of PBA [CoTCNi/HCCr]

The structural parameters of the fabricated PBA were discussed using the conventional XRD technique. As demonstrated in Fig. 1a, the PBA nanocomposite reveals diffraction peaks at $2\theta = 18.40°$, 24.60°, 36.70°, and 41.37° corresponding to the crystallographic planes (200), (220), (400), and (420), respectively, which coincide with the face-centered cubic phase of

the standard card (JCPDS No. 82-2284, space group Fm-3 m). The XRD analysis verified that there are no secondary phases arising from the starting materials. It also proves that the prepared compositions derived a monophase within the XRD detection range. As observed in Fig. 1a, all the peaks are weak, broad, and have low intensity, implying tiny crystal structure, small crystal size, and structural disorder. The XRD parameters comprising crystal size (D), dislocation density (δ), lattice strain (ε), and degree of crystallization (Xc) play a significant role in identifying the microstructure [33, 34]. Multiple defects in the crystal structure have an impact on the width and intensity of X-ray lines. These imperfections must be considered while analyzing the collected data. Crystals typically have a mosaic structure, wherein the entire crystal is partitioned into mosaic blocks measuring around 10^{-3} nm in size. Each block exhibits a structure that closely approximates an ideal configuration. However,

the blocks rotate in relation to one another at tiny angles. As a result, the mosaic crystal reflects beams over a range of angles, $\Delta(2\theta)$, in addition to Bragg's angle. One limitation that arises in relation to the size of mosaic blocks, $D_{(200)}$ and lattice strain (ε), leads to the broadening. This broadening of the peak (200) of the XRD patterns can be quantitatively characterized using Debye–Scherrer's equation formula as follows:

$$D_{(200)} = k\lambda/(\beta_{(200)} \cos\theta), \tag{1}$$

where $\beta_{(200)}$ is the full width at half maximum (FWHM) at (200) crystallographic plane in radiant, $\lambda = 1.5406$ Å is the wavelength of X-ray irradiations, $K = 0.94$ is the shape factor, and θ is the diffraction angle. The PBA (CoTCNi/HCCr) sample exhibits a finely dispersed structure and is composed of nanocrystallites that have grown together. These nanocrystallites are considered to be blocks of coherent scattering inside our material. Likewise, the dislocation density () measures the defects in crystals of nanomaterials and is defined as follows [35]:

$$\delta = \frac{1}{D_{(200)}^2}. \tag{2}$$

The lattice strain (ε) associated with the vicinity of non-uniform lattice distortions related to the variations in the d-spacing of the scattering crystals was calculated using the Stokes–Wilson equation at (400) plane:

$$\varepsilon = \frac{\beta_{(400)}}{4\tan\theta}. \tag{3}$$

The degree of crystallinity was described using the following equation:

$$X_c = \frac{0.24}{\beta}. \tag{4}$$

The XRD parameters ($D_{(200)}$, δ, ϵ, X_c) were estimated and presented in Table 1. The prepared Prussian blue analog exhibited tiny crystallite size due to the wide surface area and significant lattice strain caused by lattice defects [34–36]. Figure 1b shows the elements cobalt (Co), chromium (Cr), nickel (Ni), carbon (c), oxygen (O), and nitrogen (N) with weight percentages (wt%) of 48.65, 11.53, 7.632, 14.90, 9.968, and 7.632. The presence of an oxygen peak in the EDX spectrum without stoichiometric percent is an error

in the EDX instrument. Stoichiometry has a significant role in composite samples of metals and their oxides. The appearance of the oxygen anions and their deviation from stoichiometry can modify the charge state of the cations, which will have a major impact on the electric and dielectric characteristics of materials. This will have a significant impact on the actual application of the synthesized materials, as reported in the literature [37, 38]. The spectrum revealed the purity of the synthesized PBA with no chemical contaminants [35, 36]. Table 1 contains the concentrations of various elements. The morphological and topological nature was visualized in Fig. 2. The SEM images in Fig. 2a describe the nanoparticles in tiny spheres grown in high density without cavities. As seen, the nanoparticles are aggregated together due to the high energy on the surface. Figure 2b, c shows the 2D and 3D AFM micrographs of the powder of PBA. As observed, the surface of the powder is virtually homogenous, and the particles were defined in spherical forms evenly dispersed throughout the surface [36, 39]. The grain boundaries are clearly defined, and the grains are spherical in planes with a mean size of ~ 22 nm. The estimated values of porosity and particle count that were derived from AFM images using the SPIP program are listed in Table 1. Surface roughness is also calculated based on the estimated height deviation. Remarkable structural–morphological characteristics using an ultra-sharp tip (2 nm) of AFM micrographs revealed a uniform surface of the fabricated powder of PBA, including a high particle count, the quantum size effect, a porous surface, and an average roughness (R_s) of 6.86 nm, as illustrated in Fig. 2b, c [40, 41].

3.2 Frequency dependence of dielectric constants ε' and ε″

At various temperatures, Fig. 3a, b reveals the frequency dependency of the real and imaginary parts (ε' and ε″) of the dielectric constant. Many factors, including space charge polarization, dipolar polarization, ionic polarization, and electronic polarization, can be attributed to the reduction of ε_1 and ε_2 with frequency [42]. Moreover, at high frequencies, the values of (ε', ε″) decline until they reach a constant value. This phenomenon was caused by the dipoles' inability to follow the external field, and then the orientation polarization ceased [43]. Another observation from Fig. 3a, b is that when
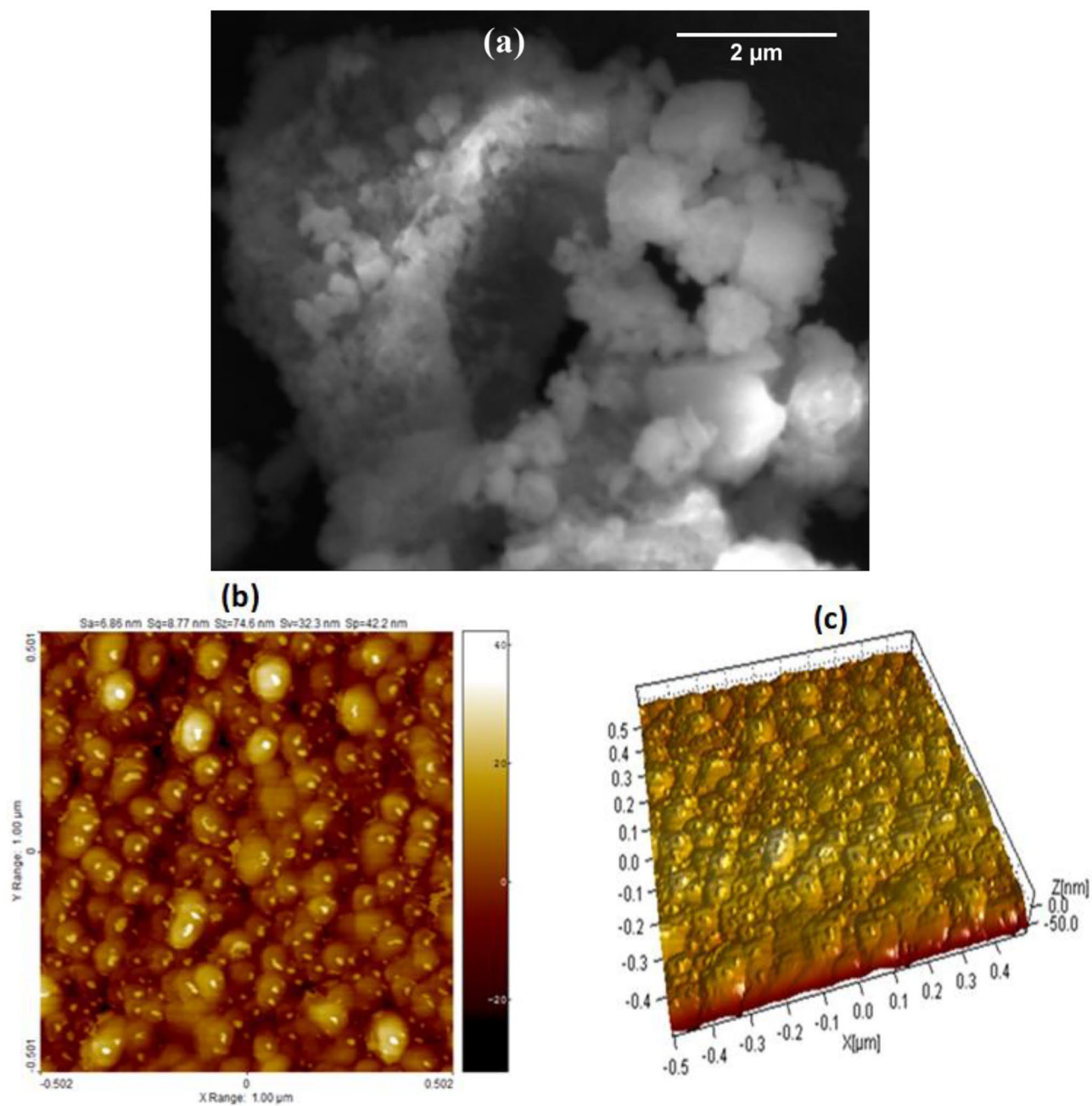
Fig. 2 **a** SEM image and **b, c** 2D and 3D AFM micrograph of the Prussian blue analog CoTCNi/HCCr

Table 1 The structural and topological parameters of the fabricated PBA CoTCNi/HCCr

Crystallographic parameters				Topological parameters			
$D_{(200)}$ (nm)	$\delta \times 10^{-3}$ (nm)$^{-2}$	$\epsilon \times 10^{-2}$	X_c	D (nm)	Particles counts	Porosity	Average roughness (R_s nm)
13.66 ± 0.30	5.35 ± 0.32	1.35 ± 0.52	14.90	22 ± 2.1	89	140	6.86
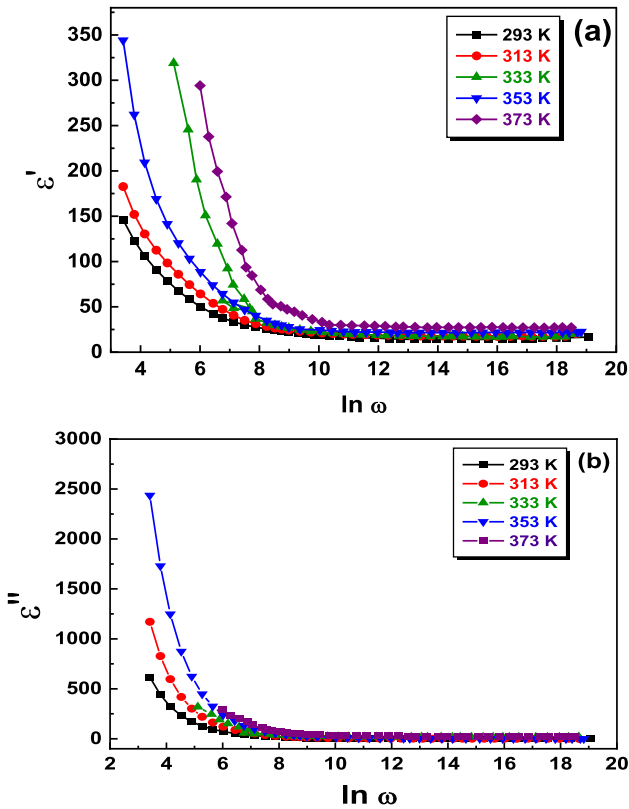
Fig. 3 a, b Frequency dependence of real and imaginary parts (ε′, ε″) of the dielectric constant of the Prussian blue analog CoTCNi/HCCr

Fig. 4 a, b Temperature dependence of real and imaginary parts (ε′ and ε″) of the dielectric constant of the Prussian blue analog CoTCNi/HCCr

temperature increases, (ε′, ε″) rises due to the stretched orientation of the dipoles, which enhances the value of orientation polarization [44, 45].

3.3 Temperature dependence of dielectric constants ε′ and ε″

Figure 4a, b demonstrates the temperature dependence of the dielectric constant ε′ and ε″. It is clear that the values of both ε′ and ε″ are nearly constants at lower temperatures. Figure 4a shows that ε′ values increment as temperature excesses occur throughout all applied frequency ranges. The rising value of ε′ can be explained by the charge carriers produced as the temperature rises. These charge carriers are easily oriented to the AC field, which influences the sample's dielectric constant [46]. Based on Fig. 4b, the dielectric loss ε″ grows with rising temperatures because of vibrational losses, conduction, and dipole contributions [46].
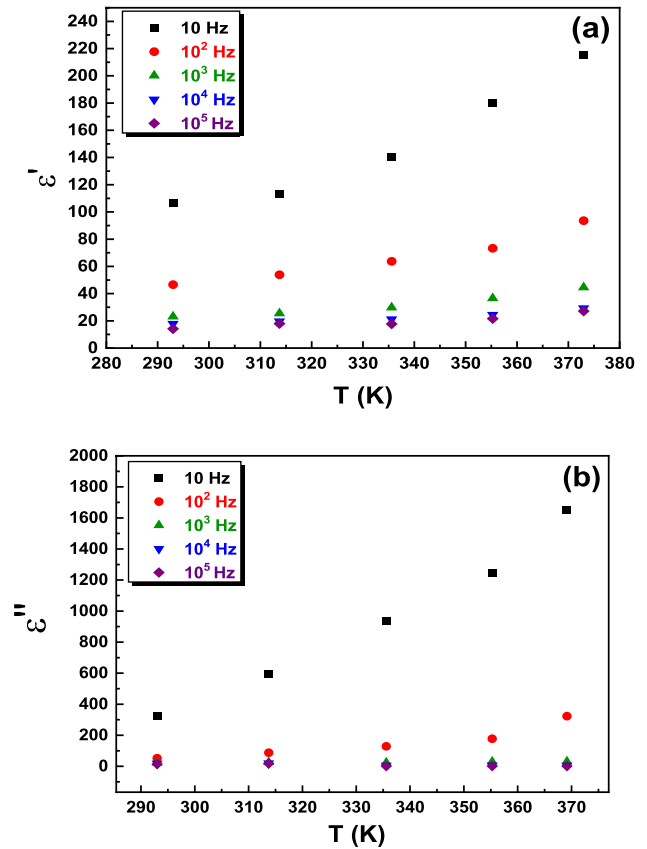
3.4 Frequency and temperature dependence of AC conductivity

The determination of AC conductivity (σ_{AC}) can be achieved by utilizing the real component of the dielectric constant, as stated in reference [42]. Figure 5 describes the frequency variation of σ_{AC} at a certain temperature for a PBA disc. As temperatures increase, the conductivity of PBA rises, confirming the sample's semiconducting characteristics [47]. At low frequencies, conductivity is nearly constant with frequency and begins growing at the hopping frequency [48]. As the temperature increases, the hopping frequency undergoes a shift towards the higher-frequency region. The determination of the exponent factor(s) at different temperatures can be achieved by employing Jonscher's power law [49]. It is found that the s values are between one and zero and that they gradually decline with temperature. The aforementioned conductive behavior is associated with the correlated
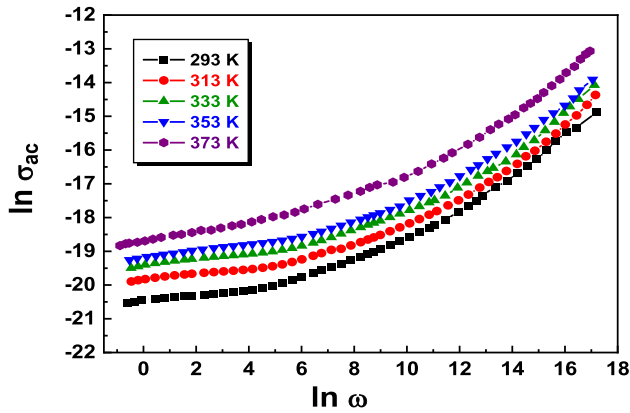
Fig. 5 The dependency of AC conductivity of PBA [$Co_{0.4}$/$(TCNi)_{0.2}$/$(HCCr)_{0.6}$] on frequency (4 Hz–100 kHz) and temperature (293–373 K)
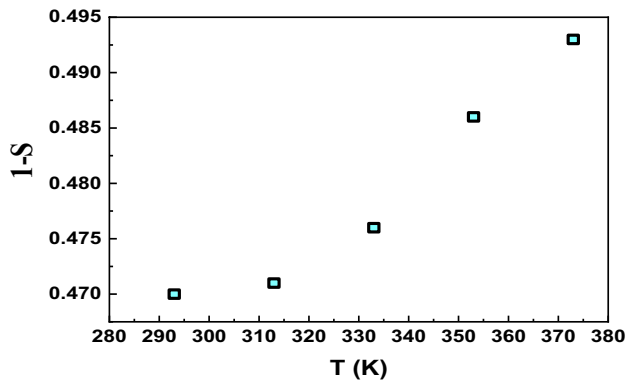

Fig. 6 The relation between (1-s) and T

barrier hopping model (CBHM) utilized in the analysis of AC conductivity [50].

The exponent factor (s) correlates to the maximum height of the hopping barrier at low temperatures (W_M) as follows:

$$s = 1 - \frac{6K_B T}{W_M}. \tag{5}$$

The determination of the W_M value was achieved by plotting the quantity of (1-s) against T, as illustrated in Fig. 6, resulting in a value of 1.69 eV. Moreover, the subsequent formula may be employed to compute the activation energy (ΔE_{ac}):

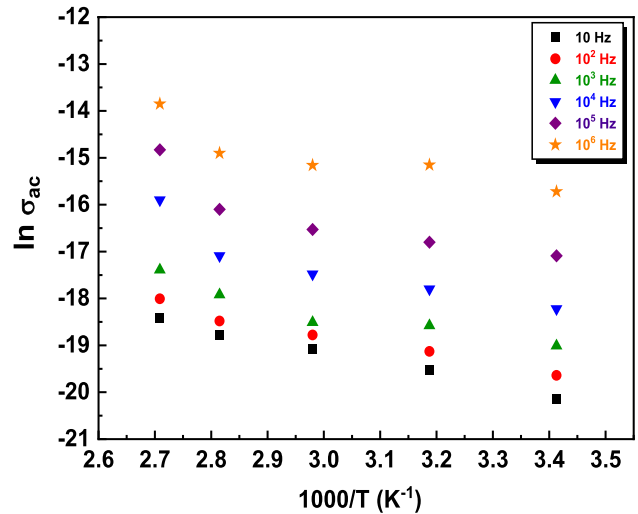$$\sigma_{ac}(\omega) = \sigma_o \exp\left[-\frac{\Delta E_{ac}}{K_B T}\right], \tag{6}$$

Fig. 7 The dependency of AC conductivity on the frequency and temperature of the Prussian blue analog CoTCNi/HCCr
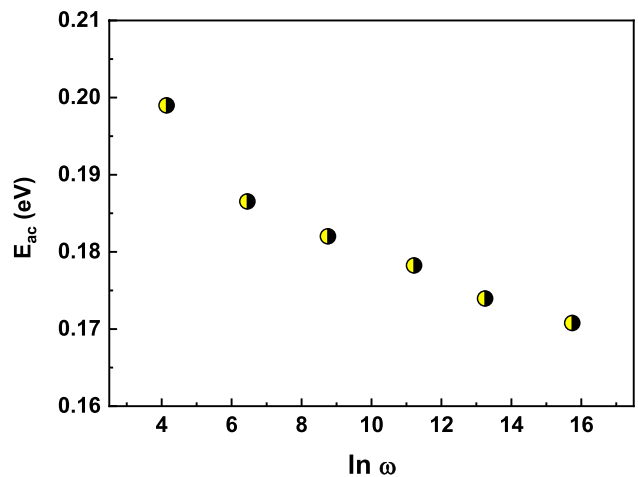

Fig. 8 The activation energy values as a function of frequencies of the Prussian blue analog CoTCNi/HCCr

where σ_o is the pre-exponential factor, σ is the activation energy, and k is the Boltzmann constant.

At various frequencies, the temperature dependency of $\sigma_{ac}(\omega)$ of the PBA sample is apparent in Fig. 7. According to the graph, $\sigma_{ac}(\omega)$ grows linearly with temperature. The observed phenomenon suggests that the conductivity can be attributed to a thermally stimulated mechanism that originates from discrete localized states within the gap [51]. The ΔE_{ac} values have been estimated from Fig. 7 according to Eq. 6. According to the findings presented in Fig. 8, there is a noticeable decrease in ΔE_{ac} as the frequency increases. This trend can be explained by the impact of frequency on the conduction process

mechanism, as noted by previous research [51]. Consequently, with higher-frequency applications, there are more electron hops between localized states. According to previous studies, this result is very consistent [52, 53].

3.5 Complex dielectric modulus

The complex dielectric modulus must be examined in order to evaluate the electrical transport mechanism and know how it affects localized dielectric relaxation [54]. Equations (7, 8) may be utilized to derive the real M′ and imaginary M″ components of the electric modulus.

$$M'(\omega) = \frac{\varepsilon'}{\varepsilon'^2(\omega) + \varepsilon''^2(\omega)} \quad (7)$$

$$M''(\omega) = \frac{\varepsilon''}{\varepsilon'^2(\omega) + \varepsilon''^2(\omega)}. \quad (8)$$

Figure 9a, b depicts the investigation of M″ and M′ at different temperatures, with frequency as the independent variable. At lower frequencies, the magnitudes of M′ and M″ tend towards zero, which can be attributed to the elevated capacitance, as reported in the literature [55]. Furthermore, the parameter "M" exhibits a peak value that undergoes a positive displacement towards higher frequencies with an increase in temperature. Before M″ reaches its maximum value at lower frequencies, mobile charge carriers across great distances are observable. Nevertheless, at higher frequencies, beyond M′ maximum value, restricted carriers exhibit potential well, causing them to be mobile over short distances [56].

3.6 The Cole–Cole graph of complex impedance

The technique of impedance spectroscopy is widely recognized as a means of assessing the dielectric characteristics of a given material. Figure 10 depicts the Nyquist plot of the complex impedance's real (Z′) and imaginary (Z″) components at different temperatures. This Cole–Cole graph offers considerable and reliable data on solid electrolyte conductivity. The formulae (9, 10) can be used to get Z′ and Z″:
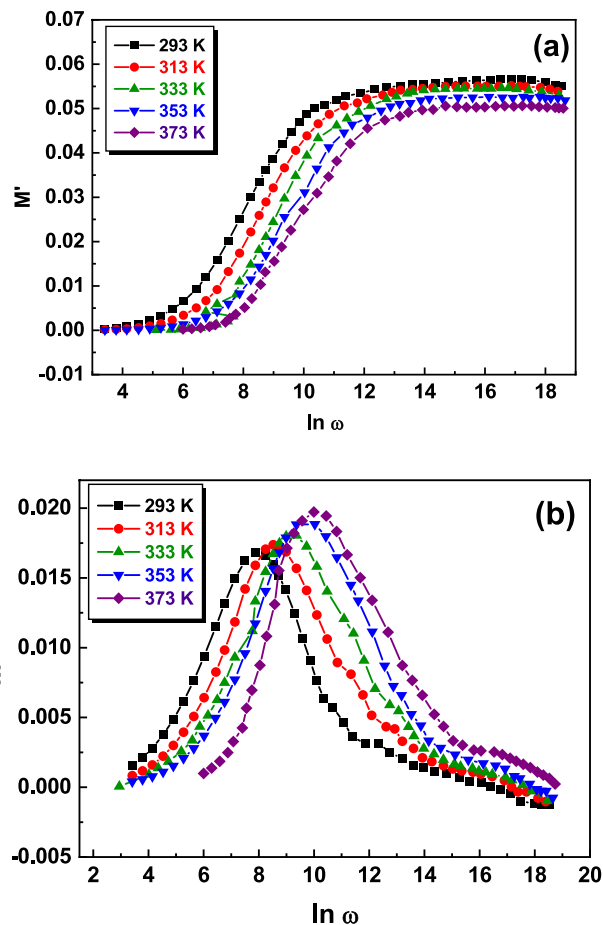
$$z' = \frac{G}{G^2 + \omega^2 C_p^2} \quad (9)$$

Fig. 9 **a, b** The variation of **a** real part M′ (ω), and **b** imaginary part, M″ (ω), of the electric modulus versus ln ω at various temperatures of the Prussian blue analog CoTCNi/HCCr
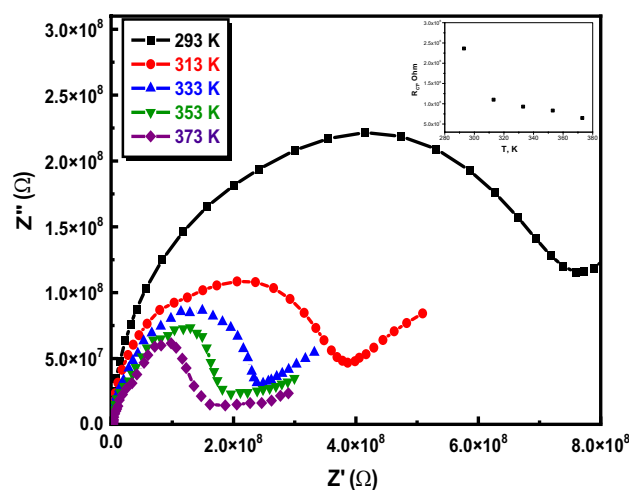

Fig. 10 The Nyquist curve for the real, Z′, and imaginary, Z″, parts of the complex impedance at various temperature of the Prussian blue analog CoTCNi/HCCr
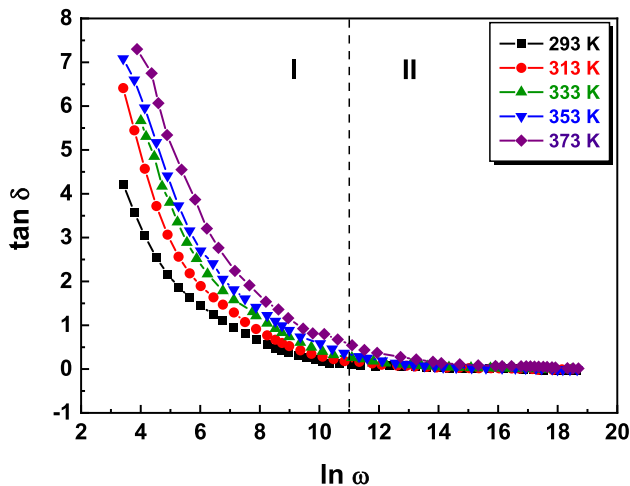
Fig. 11 The change of the tan δ as a function of angular frequency at various temperatures of the Prussian blue analog CoTCNi/HCCr

$$z'' = \frac{\omega C_p^2}{G^2 + \omega^2 C_p^2}' \tag{10}$$

where C_p and G denote the observed parallel capacitance and conductance. The semi-circle's radius in the given figure represents the grain boundary resistance at low frequencies. In contrast, the radius of the semicircle at high frequencies signifies the grain resistance, as reported in the literature [57]. The estimation of the charge transfer resistance, R_{ct}, can be facilitated by utilizing the diameter of the semi-circle present in the Nyquist impedance plot. As shown in the inset of Fig. 10, R_{ct} decreases considerably as the temperature rises. This finding can be interpreted by the reduction in the blocking effect, which most likely occurred at the semiconductor and metal interface owing to the variation in the work functions of the semiconductor and metal [58].

The loss tangent, denoted as tan δ, is an essential parameter that characterizes the energy dissipation of a material under varying temperatures. The parameter is derived through computation involving the two designated dielectric constants (ε′ and ε″), as expressed by the subsequent formula [59].

$$\tan \delta = \frac{\varepsilon''}{\varepsilon'}. \tag{11}$$

Figure 11 illustrates the variation of tanδ with respect to angular frequency at different temperatures. It has been demonstrated that tan δ increases with

rising temperatures; nonetheless, tanδ is inversely correlated to angular frequency [46]. In region I, when temperature values rise, more holes and electrons can be generated that can be oriented with a low switching frequency. The value of tanδ shows a significant decrease with increasing frequency (region II), with a small influence of the applied electric field (AC). The observed phenomenon can be attributed to the high frequency switching of the applied field, which impedes the mobility of charge carriers in response to field fluctuations [46]. The annealing process is expected to have significant effects on the increase in the crystallite size and size distribution of the obtained PBA, leading to observable changes in its electrical characteristics [60]. Conversely, annealing has a significant impact on the enhancement of both AC conductivity and dielectric constant values, and hence changed the loss tangent tanδ. The observed phenomenon may be attributed to the simultaneous effects of increased holding time and elevated heating temperature. Therefore, the pre-existing dislocations present at the grain borders are effectively counteracted, thus facilitating unconstrained grain boundary expansion [60, 61].

4 Conclusion

Prussian blue analog (PBA) is receiving increasing interest in the field of energy storage, such as their high specific capacity, ease of synthesis, as well as low cost. A chemical co-precipitation method was employed to synthesize the $Co_{0.4}[Ni(CN)_4]_{0.2}/[Cr(CN)_6]_{0.6}$ Prussian blue analog. Based on the microstructural properties analyzed through XRD and EDX, it can be implied that the nanocomposite exhibits low crystallinity and a small crystallite size (13.66 ± 0.32 nm). The micrographs acquired through the utilization of SEM and AFM techniques have demonstrated that the particles exhibit a consistent spherical morphology and enhanced density. The findings of this investigation indicate that an increase in frequency is associated with a decrease in activation energy. This phenomenon can be attributed to the impact of frequency on the conduction mechanism. On the other hand, the characteristics of s values offer validation for the correlated barrier hopping model (CBHM) regarding AC conductivity. The dielectric constant's temperature and frequency

dependence are expressed through its real and imaginary components, denoted as ε' and ε'', correspondingly. The trend that has been observed suggests a negative correlation between the values of ΔE_{ac} and frequency, while the values of R_{ct} demonstrate a negative association with temperature. Empirical evidence has shown that tan δ exhibits a positive correlation with increasing temperatures. However, it should be noted that there exists an inverse relationship between tan δ and angular frequency. In the first region, an increase in temperature results in the generation of additional holes and electrons that exhibit a low switching frequency when oriented. The observed trend in the value of tanδ indicates a notable reduction as the frequency increases, which is observed in region II. Additionally, the effect of the applied electric field (AC) on this trend is relatively minor. The identified phenomenon can be attributed to the rapid oscillation of the applied field at a high frequency, which hinders the movement of charge carriers in reaction to fluctuations in the field.

Acknowledgements

Author contribution

All authors have participated in the conception, analysis, and interpretation of the data. The authors have participated in revising it critically for important intellectual content and approval of the final version.

Funding

Data availability

All authors declare the data at the heart of the research article is the authors' original data; these data have not received prior publication and are not under consideration for publication elsewhere.

Declarations

Conflict of interest All authors declare that they have no conflicts of interest, and the article is the author's original work, has not received prior publication, and is not under consideration for publication elsewhere. We are stating that this manuscript has not been submitted to, nor is it under review at another journal or other publishing venue. Also, the authors have no affiliation with any organization with a direct or indirect financial interest in the subject matter discussed in the manuscript.

References

1. V.A. Turchenko, A.V. Trukhanov, I.A. Bobrikov, S.V. Trukhanov, A.M. Balagurov. Crystallogr. Rep. **60**, 629–635 (2015)
2. M.V. Zdorovets, A.L. Kozlovskiy, D.I. Shlimas, D.B. Borgekov, J. Mater. Sci. **32**, 16694–16705 (2021)
3. D.A. Vinnik, V.E. Zhivulin, D.A. Uchaev, S.A. Gudkova, D.E. Zhivulin, A.Y. Starikov, S.V. Trukhanov, V.A. Turchenko, T.I. Zubar, T.P. Gavrilova, R.M. Eremina, E. Fadeev, E. Lähderanta, A.S.B. Sombra, D. Zhou, R.B. Jotania, C. Singh, A.V. Trukhanov, J. Alloys Compd. **859**, 158365 (2021)
4. A.V. Trukhanov, K.A. Darwish, M.M. Salem, O.M. Hemeda, M.I. Abdel Ati, M.A. Darwish, E.Y. Kaniukov, S.V. Podgornaya, V.A. Turchenko, D.I. Tishkevich, T.I. Zubar, K.A. Astapovich, V.G. Kostishyn, S.V. Trukhanov, J. Alloys Compd. **866**, 158961 (2021)

5. J. Brown, Observations and experiments upon the foregoing preparation. Philos. Trans. **33**, 19–24 (1724)

6. L. Boudjema, J. Long, F. Salles, J. Larionova, Y. Guari, P. Trens, Chem. Eur. J. **25**, 479–484 (2019)

7. Yen-Hsin, Chiang, Earth Environ. Sci. **384**, 012005 (2019)

8. E. Karyakina, Anal. Chem. **67**, 2419–2423 (1995)

9. Y. Xu, S. Zheng, H. Tang, X. Guo, H. Xue, H. Pang, Energy Storage Mater. **9**, 11–30 (2017)

10. B. Wang, Y. Han, X. Wang, N. Bahlawane, H. Pan, M. Yan, Y. Jiang, IScience **3**, 110–133 (2018)

11. O. Sato, Y. Einaga, T. Iyoda, A. Fujishima, K. Hashimoto, J. Phys. Chem. B **101**, 3903–3905 (1997)

12. O. Sato, Y. Einaga, A. Fujishima, K. Hashimoto, Inorg. Chem. **38**, 4405–4412 (1999)

13. J.H. Park, Y.D. Huh, E. Cizmar, S.G. Gamble, D.R. Talham, M.W. Meisel, J. Magn. Magn. Mater. **272**, 1116–1117 (2004)

14. X.P. Shen, S.K. Wu, Y. Liu, K. Wang, Z. Xu, W.J. Liu, Colloid Interface Sci. **329**, 188–195 (2009)

15. J.C. Wojdel, I.D.R. Moreira, S.T. Bromley, F. Illas, J. Mater. Chem. **19**, 2032–2036 (2009)

16. J.N. Behera, D.M. D'Alessandro, N. Soheilnia, J.R. Long, Chem. Mater. **21**, 1922–1926 (2009)

17. D.G. El-Damhogi, H.M. El-Mallah, Elesh, Opt. Quant. Electron. **52**, 429 (2020)

18. D.H.M. Buchold, C. Feldmann, Chem. Mater **19**, 3376–3380 (2007)

19. S. Ohkoshi, T. Nuida, T. Matsuda, H. Tokoro, K. Hashimoto, J. Mater. Chem. **15**, 3291–3295 (2005)

20. A.V. Trukhanov, N.A. Algarou, Y. Slimani, M.A. Almessiere, A. Baykal, D.I. Tishkevich, D.A. Vinnik, M.G. Vakhitov, D.S. Klygach, M.V. Silibin, T.I. Zubar, S.V. Trukhanov, RSC Adv. **10**, 32638 (2020)

21. A.L. Kozlovskiy, M.V. Zdorovets, Mater. Chem. Phys. **263**, 124444 (2021)

22. O.S. Yakovenko, L.Y. Matzui, L.L. Vovchenko, V.V. Oliynyk, V.V. Zagorodnii, S.V. Trukhanov, A.V. Trukhanov, Nanomaterials. **11**, 2873 (2021)

23. A.V. Trukhanov, D.I. Tishkevich, S.V. Podgornaya, E.Y. Kaniukov, M.A. Darwish, T.I. Zubar, A.V. Timofeev, E.L. Trukhanova, V.G. Kostishyn, S.V. Trukhanov, Nanomaterials. **12**, 868 (2022)

24. T.I. Zubar, S.A. Sharko, D.I. Tishkevich, N.N. Kovaleva, D.A. Vinnik, S.A. Gudkova, E.L. Trukhanova, E.A. Trofimov, S.A. Chizhik, L.V. Panina, S.V. Trukhanov, A.V. Trukhanov, J. Alloys Compd. **748**, 970–978 (2018)

25. A.L. Kozlovskiy, M.V. Zdorovets, J. Mater. Sci. **30**, 11819–11832 (2019)

26. H.M. El-Mallah, M.A.-E. Salam, D.G. El-Damhogi, E. Elesh, Radiat. Phys. Chem. **176**, 109012 (2020)

27. G.D. Rees, R. Evans-Gowing, S.J. Hammond, B.H. Robinson, Langmuir **15**, 1993–2002 (1999)

28. A.L. Kozlovskiy, A. Alina, M.V. Zdorovets, J. Mater. Sci. **32**, 3863–3877 (2021)

29. R.E. El-Shater, H. El Shimy, S.A. Saafan, M.A. Darwish, D. Zhou, K.C.B. Naidu, M.U. Khandaker, Z. Mahmoud, A.V. Trukhanov, S.V. Trukhanov, F. Fakhry, Mater. Adv. **4**, 2794–2810 (2023)

30. M. Taguchi, K. Yamada, K. Suzuki, O. Sato, Y. Einaga, Chem. Mater. **17**, 4554–4559 (2005)

31. J.H. Yang, H.S. Wang, L.H. Lu, W.D. Shi, H.J. Zhang, Cryst. Growth Des. **6**, 2438–2440 (2006)

32. X.L. Wu, M.H. Cao, C.W. Hu, X.Y. He, Cryst. Growth Des. **6**, 26–28 (2006)

33. X. Tu, Y. Liu, K. Wang, Z. Ding, X. Xu, T. Lu, L. Pan, J. Colloid Interface Sci. **642**, 680–690 (2023)

34. Y. Jiajia Han, H.Q. Han, X. Liu, C. Wang, J. Alloys Compd. **950**, 169928 (2023)

35. X. Wei Wang, H. Yu, Y. He, Y. Wang, L. Li, Y.-N. Deng, Liu, Chem. Eng. J. **465**, 142865 (2023)

36. Elsayed, Elgazzar, Mater. Res. Express. **7**, 075004 (2020)

37. S.V. Trukhanov, A.V. Trukhanov, H. Szymczak, Low Temp. Phys. **37**, 465–469 (2011)

38. A. Kozlovskiy, K. Egizbek, M.V. Zdorovets, M. Ibragimova, A. Shumskaya, A.A. Rogachev, Z.V. Ignatovich, K. Kadyrzhanov, Sensors. **20**, 4851 (2020)

39. Y.-C. Trakarn Yimtrakarn, A. Liao, M.V. Sanin, J.-L. Chen et al., Mater. Today Commun. **34**, 105231 (2023)

40. M. Elsayed Elgazzar, Ahmed, M.M. Abdel-Raoof, Abdul-Aziz, A.M. El-Attar, S.A. Ashmawy, Abdulla, Microchem. J. **178**, 107413 (2022)

41. Y. Mengting, L. Yang, L.Y.T. Wang, Y. Wang, Y. Qin et al., Int. J. Biol. Macromol. **231**, 123293 (2023)

42. A.A.A. Darwish, E.F.M. El-Zaidia, M.M. El-Nahass, T.A. Hanafy, A.A. Al-Zubaidi, J. Alloy Compd. **586**, 393 (2014)

43. I. Saleem, A.A.A. Qashoua, M. Darwisha, Z. Rashada, Khattari, Phys. B **525**, 159–163 (2017)

44. A.A. Dakhel, J. Phys. Chem. Solids. **65**, 1765 (2004)

45. M. Dongol, M.M. El-Nahass, A. El-Denglawey, A.A. Abuelwafa, T. Soga, Chin. Phys. B **25**, 067201 (2016)

46. Z.A. Alrowaili, A. Qasem, E.R. Shaaban, M. Ezzeldien, Physica B **612**, 412975 (2021)

47. C. Thirmal, S.D. Ramarao, L. Srinivasa Rao, V.R.K. Murthy, Mater. Res. Bull. **146**, 111618 (2022)

48. S. Sumi, P.P. Rao, M. Deepa, P. Koshy, J. Appl. Phys. **108**, 63718 (2010)

49. A.K. Jonscher, Nature **267**(5613), 673 (1977). https://doi.org/10.1038/267673a0.s2CID4179723

50. E. El-Menyawy, H. Zeyada, M. El-Nahass, Solid State Sci. **12**, 2182 (2010)

51. M. El-Nahass, E.M. Mossad, A. Farag, S. Menshawy, F. Abu-Samaha, E. Elesh, IOSR J. Appl. Phys. **6**, 22–29 (2014)

52. A. Tabib, N. Sdiri, H. Elhouichet, M. Fe´rid, J. Alloy Compd. **622**, 687 (2015)

53. E. Elesh, Z. Mohamed, M.S. Dawood, J. Electron. Mater. **49**, 2633–2641 (2020)

54. B. Shri Prakash, K.B.R. Varma, Phys. B **9**, 382:312 (2006)

55. A.S.A. Khiar, R. Puteh, A.K. Arof, Phys. B **373**, 23 (2006)

56. A. Moguš-Milankovic, A. Šantic, V. Licina, D.E. Day, J. Non-Cryst Solids. **351**, 3235 (2005)

57. C. Thirmal, P. Murugavel, V. Subramanian, Curr. Appl. Phys. **14**, 688–690 (2014)

58. M.M. El-Nahass, H.S. Metwally, H.E.A. El-Sayed, A.M. Hassanien, Mater. Chem. Phys. **133**, 649 (2012)

59. I. Bunget, M. Popescu, Physics of solid dielectrics. Mater. Sci. Monogr. **19**, 443 (1984)

60. S.V. Trukhanov, L.S. Lobanovski, M.V. Bushinsky, V.A. Khomchenko, V.V. Fedotova, I.O. Troyanchuk, H. Szymczak, Semiconductors **41**, 507–511 (2007)

61. A.L. Kozlovskiy, M.V. Zdorovets, J. Mater. Sci. **31**, 11227–11237 (2020)